

Ambient N≡N bond weakening hydrogenation by utilizing the highly defective Cu₃BiS₃/MnO₂ electrocatalyst for ammonia yield above 3 mg/h·cm²: The N₂-nano dipole interaction micromechanism

Merga Hailemariam Urgesa ^a, Dong-Hau Kuo ^{a,b,*}, Tadele Negash Gemedo ^a, Quoc-Nam Ha ^a, Noto Susanto Gultom ^a

^a Department of Material Science and Engineering, National Taiwan University of Science and Technology, Taipei 10607, Taiwan

^b Graduate Institute of Energy and Sustainability Technology, National Taiwan University of Science and Technology, Taipei 10607, Taiwan



ARTICLE INFO

Keywords:

Electrochemical reaction
Cu_{3-x}BiS₃/MnO_{2-y}
Nitrogen fixation
Ammonia
Nano dopole
N₂ hydrogenation

ABSTRACT

This study introduces a novel Cu₃BiS₃/MnO₂ composite catalyst for the electrochemical nitrogen reduction reaction (eNRR) to address challenges in sustainable ammonia production, aiming to replace the energy-intensive Haber-Bosch process. The ternary Cu₃BiS₃/MnO₂ catalyst exhibited impressive results, achieving a high ammonia yield rate of 3604 µg h⁻¹cm⁻² and a significant Faradaic efficiency of 31.4 % at -0.75 V vs. RHE in a 0.5 M Na₂SO₄ solution, while only 446 µg h⁻¹cm⁻² from binary metal CuMn(2:3). This success was attributed to abundant cation and anion defects with multiple valence charges in the Cu_{3-x}BiS₃/MnO_{2-y} catalyst, created by introducing the third metal, Bi, into the binary CuMn system. These defects served as trapping centers for dynamic nitrogen molecule activation and facilitated charge transport, enhancing the eNRR process. This study underscores the potential of highly defective Cu_{3-x}BiS₃/MnO_{2-y} as an efficient and sustainable catalyst for electrochemical nitrogen fixation, offering a greener approach to ammonia production.

1. Introduction

Environmental pollution and energy shortages have emerged as two main obstacles to sustainable development due to the rapid population rise and expansion of global industrialization [1]. The growing fossil fuel usage has worsened these problems [2]. Ammonia (NH₃) has emerged as a possible option in this environment, and developing new energy sources is essential [3]. Ammonia has benefits such as a low air-fuel ratio, a low rate of heat loss, and no carbon dioxide emissions during burning [4,5]. Additionally, it is more practical than hydrogen in the upcoming energy system because it is simple to liquefy, store, and transport [6,7]. NH₃ manufacture, however, has been very difficult due to its easily escaped gas state and triple-bond inertness [5]. The traditional process, the Haber-Bosch reaction, uses much energy and emits many greenhouse gases [8]. Therefore, creating ammonia synthesis technologies that are low-energy consumption and environmentally benign is critical.

Among the various approaches, electrochemical nitrogen reduction reaction (eNRR) technology has gained significant attention due to its

environmental friendliness and lack of pollution [9,10]. However, it faces challenges due to slow reaction kinetics from weak nitrogen adsorption and a high activation barrier [11]. The Hydrogen Evolution Reaction (HER) competes with eNRR for protons and electrons, potentially reducing the efficiency of nitrogen reduction to ammonia due to their similar proton reduction mechanisms, consequently leading to unsatisfactory Faradaic efficiency (FE) [12–14]. For overcoming the barrier, catalysts play a crucial role in efficient eNRR conducted under ambient conditions [15,16]. Various strategies have been explored, including precious metal deposition on catalyst surfaces [17,18], the construction of composite catalysts and defect engineering at the interfaces of heterogeneous structures [19], metal/nonmetal doping [20], and the engineering of surface oxygen vacancies [21]. Metal/nonmetal doping introduces additional active sites and alters electronic properties, while surface oxygen-vacancy engineering enhances catalytic performance by creating defect sites [22]. These interfaces act as active sites that enable charge separation and electron transfer during the reaction [23,24]. While noble metal catalysts like Ag, Au, Pd, Rh, and Ru exhibit favorable catalytic activities for eNRR, their limited availability and

* Corresponding author at: Department of Material Science and Engineering, National Taiwan University of Science and Technology, Taipei 10607, Taiwan.
E-mail address: dhkuo@mail.ntust.edu.tw (D.-H. Kuo).

high cost hinder large-scale industrialization [25]. R. Hao prepared single-atom Pt/WO₃ to reach NH₃ yield of 342.4 µg h⁻¹ mg_{cat}⁻¹ or 10.27 µg h⁻¹ cm⁻² and FE of 31.1 % [26]. Lv et al. reported the laser-synthesized TiO_x deposited with hydrothermal Pt to achieve NH₃ yield of 2520 µg h⁻¹ mg_{cat}⁻¹ or 91.0 µg h⁻¹ cm⁻² and FE of 1.57 % [27]. Y. Chen synthesized single-atom Ag/N-doped carbon with NH₃ yield of 270.9 µg h⁻¹ mg_{cat}⁻¹ or 54.2 µg h⁻¹ cm⁻² and FE of 21.9 % [28].

Bismuth-based materials have emerged as a promising catalyst for nitrogen reduction (NRR) [29]. Its unique attributes including limited surface electron availability and weak hydrogen bonding, and effective suppression for the competing hydrogen evolution reaction (HER) [30]. Through robust interaction between Bi 6p orbitals and N 2p orbitals, N₂ adsorption and activation on Bi surfaces are greatly enhanced, resulting in superior NRR selectivity and activity compared to traditional transition metals [30,31]. Moreover, the introduction of high concentrations of potassium ions in the electrolyte stabilizes pivotal nitrogen-reduction intermediates, thereby amplifying Faradaic efficiency [30,32]. Further optimization strategies, such as adjusting catalyst hydrophilicity and fostering plentiful three-phase boundaries, bolster ammonia yield and Faradaic efficiency [33]. Bismuth-based catalytic prowess is also underscored by its ability to efficiently convert N₂ to NH₃, with pronounced selectivity and efficiency, while mitigating competing reactions like HER or ORR [29,34]. Its capacity for nitrogen reduction at low overpotentials underscores its energy efficiency, a pivotal aspect in advancing eNRR systems [35]. Moreover, the inherent stability of bismuth compounds under requisite conditions renders them well-suited for enduring operation in electrochemical cells, fortifying the durability and reliability of bismuth-based eNRR catalysts [36].

Noble metal-free oxide/oxide, oxide/sulfide, and sulfide/sulfide have emerged as promising alternatives due to their abundance and respectable catalytic performance [37–40]. Y. Liu et al. developed BiVO₄/TiO₂ nanotube heterojunction composite with rich oxygen vacancies to have an NH₃ yield of 8.54 µg h⁻¹ cm⁻² and FE of 7.7 % [37]. X. Zi et al. prepared S-vacancy 1 T MoS₂ on MoO₃ support to perform NH₃ yield of 116.1 µg h⁻¹ mg_{cat}⁻¹ or 41.47 µg h⁻¹ cm⁻² and FE of 18.9 % [38]. T. Jiang et al. prepared 2D-MoS₂ on Cu_{2-x}S quantum dots by thermal chemical precipitation to reach NH₃ yield of 22.1 µg h⁻¹ mg_{cat}⁻¹ or 1.77 µg h⁻¹ cm⁻² and FE of 6.06 % [39]. B. Wang et al. synthesized FeS₂/MoS₂ by hydrothermal method to yield NH₃ at 2.59 µmol h⁻¹ mg⁻¹ or 4.40 µg h⁻¹ cm⁻² and a FE of 4.63 % [40]. Here, there are two points to be noted. One is noting the unit of the NH₃ yield a matter for comparison and the other is the difficulty in achieving a high NH₃ yield. By employing different material strategies, researchers aim to overcome the limitations of eNRR and develop efficient, sustainable, and economically viable ammonia synthesis technologies by employing precious metal deposition, composite catalyst construction, metal/nonmetal doping, surface oxygen vacancy engineering, etc. While CuMn metallic alloy was evaluated at a NH₃ rate of 28.9 µg h⁻¹ cm⁻² with FE of 9.83 % [41], the Cu-Mn-Bi-formed Cu₃BiS₃/MnO₂ sulfide/oxide catalyst has not yet been reported.

Recently, our group synthesized all-oxide (Fe,Mn,Ga)₃O_{4-x}/(Mn,Fe)₂O_{3-y} composite catalyst to upgrade the NH₃ yield to 814 µmol h⁻¹ mg_{cat}⁻¹ or 2036 µg h⁻¹ cm⁻² and a FE of 5.77 % [42]. More than 25 times higher in yield rate was achieved by adding the third metal precursors to form the ternary metal compound system. To further support the concept of highly defective composite catalysts for eNRR by adding a third metal precursor, a novel Bi-added Cu-Mn sulfide/oxide composite system is demonstrated here. In this study, we focused on developing a charged defects-filled Cu_{3-x}BiS₃/MnO_{2-y} electrocatalyst system with great promise for advanced electrochemical catalytic nitrogen conversion, by adding the third metal Bi precursor to interrupt the phase-formation reactions and crystallization. This study aims to develop an efficient and sustainable ammonia production process by addressing the urgent need for an alternative nitrogen economy.

2. Experimental part

2.1. Synthesis of Cu₃BiS₃/MnO₂

There are multiple steps involved in the hydrothermal synthesis of a ternary material. First, the Nickel foam (NF) was processed by cutting it into 1 × 1 cm² pieces and washing it to remove the oxide layer on the surface, which was accomplished by soaking it in 3 M HCl solution and ultrasonically treating it for 30 min. The NF was then treated with ethanol while being cleaned with ultrasonic energy for 30 min and then rinsed with deionized water. It was then dried at 105 °C for 2.5 h in an oven.

To synthesize Cu₃BiS₃/MnO₂, a simple one-step hydrothermal process was employed. In this process, 2 mmol of Bi(NO₃)₃·5 H₂O is dissolved in a 30 mL solution of HNO₃ in the first beaker. The solution was then sonicated for 1 h. In a separated reactor, a solution containing 2 mmol of Mn(NO₃)₂·4 H₂O, 3 mmol of Cu(NO₃)₂, and 5 mmol of thiourea were prepared by dissolving them in 15 mL of deionized water. After 30 min of stirring, this solution was injected into the first beaker. The solution was mixed and then the pH value was adjusted to 7 using NH₄OH. Then, four pieces of Ni foam at a dimension of 1 × 1 cm² were added to the solution. The mixture was subsequently transferred to a Teflon-lined autoclave and heated at 160 °C for 16 h. After cooling to room temperature naturally, the obtained products were washed with distilled water and ethanol several times and then dried in an oven at 70 °C for 2 h. The procedure is schematically shown in Scheme 1.

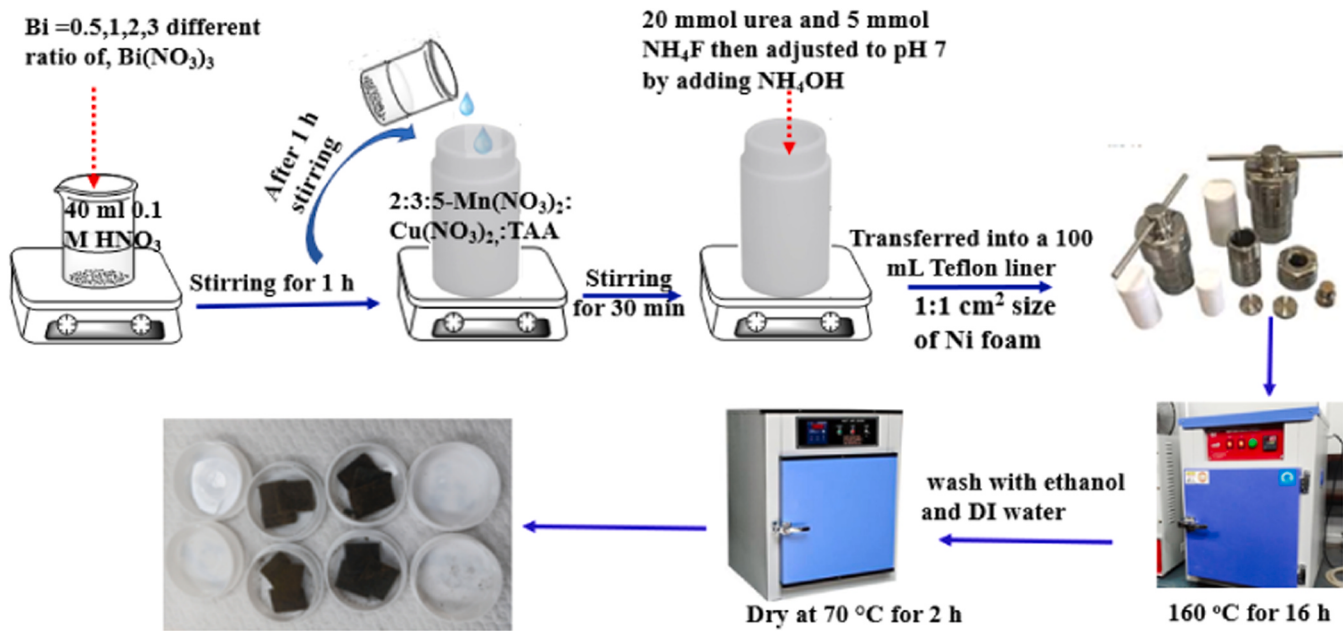
Similar procedures were followed for preparing other systems with different combinations of Cu, Mn, and Bi ratios, such as 3:2:0.5, 3:2:1, 3:2:2, and 3:2:3. The binary metal sulfide/oxide systems were also prepared for comparison purposes, as indicated in Table S1. The mass loading of the catalyst on the Ni foam was determined by measuring the weight difference before and after synthesis, which averages approximately 2.51 mg.

2.2. Evaluation of electrochemical nitrogen fixation

In the N₂ reduction experiments, a two-compartment cell was used under ambient conditions, with a Nafion 211 membrane separating the compartments. Before conducting the experiments, the Nafion 211 membrane was subjected to pretreatment, which was performed in a 5 % H₂O₂ solution and then with 10 % H₂SO₄ for 1 h each at 80 °C. Subsequently, it was rinsed with deionized water for an additional hour.

The electrochemical measurements were performed using a potentiostat Biologic SP-300 Science instrument. A three-electrode system was employed, consisting of a Pt electrode as the counter electrode, Ag/AgCl (saturated KCl electrolyte) as the reference electrode, and the as-synthesized material of 1 × 1 cm² area with ~ 2.5 mg mass loading as the working electrode. The potentials were referenced against the reversible hydrogen electrode (RHE) using E vs. RHE = E vs. Ag/AgCl + 0.059 pH + E°_{Ag/AgCl}, where the potential E°_{Ag/AgCl} equals 0.1976 V at 25 °C. For the N₂ reduction experiments, chronoamperometry tests were conducted in an N₂-saturated 0.5 M Na₂SO₄ solution (75 mL). The Na₂SO₄ electrolyte was purged with Ar for 30 min before the measurements. Pure N₂ gas with a purity of 99.99 % was introduced into the cathodic compartment at a flow rate of 80 mL min⁻¹, ensuring complete coverage of the cathode by the gas bubbles. For evaluating the production performance, the electrolyte was replaced every 2 h without making any changes to the electrode or Nafion membrane.

The method for determining Ammonia (NH₃) was described as follows. During the electrochemical nitrogen reduction reaction (eNRR), the sample was allowed to sit for 2 h. Nessler reagents were added by taking 5 mL of sample per 30 min, and the UV-visible absorption spectrum was measured in yellow-orange color (Fig. S1). The concentration-absorbance curves were calibrated using a standard NH₄Cl solution with various concentrations. The following equations, Eqs. (1) and (2) were utilized to calculate the NH₃ yield and the



Scheme 1. Diagrammatic representation for synthesizing the CuMnBi (3:2; X= 0.5, 1, 2, and 3) heterojunction structure.

corresponding percentage of Faradaic efficiency (FE):

$$\text{NH}_3\text{yield} = \frac{\text{C}_{\text{NH}_3} \times V}{t \times A} \quad (1)$$

$$\% \text{FE} = \frac{3 \times F \times \text{C}_{\text{NH}_3} \times V}{17 \times Q} \times 100\% \quad (2)$$

where C_{NH_3} (mg L^{-1}) is the measured NH_3 concentration, V (mL) is the volume of the electrolyte, t (h) is the reduction time, A (cm^2) is the area of nickel foam used, or m (mg) is the mass loading of the catalyst on Ni foam used, F (96500 C mol $^{-1}$) is the Faradaic constant, and Q (C) is the quantity of applied electricity. The possible by-product N_2H_4 was detected using the Watt and Chrissp method of H_2SO_4 with KMnO_4 .[43]

2.3. Characterizations

The as-synthesized material was subjected to various characterization techniques. X-ray diffraction (XRD) pattern was obtained using a Bruker D2 phaser diffractometer with Cu K α radiation ($\lambda = 1.5418 \text{ \AA}$). The surface morphology and microstructure were investigated using a field-emission scanning electron microscope (FE-SEM) model JSM 6500 F from JEOL, Tokyo, Japan, and a high-resolution transmission electron microscope (HR-TEM) model JEOL-2100 from JEOL, USA. X-ray photoelectron spectroscopy (XPS) analysis was conducted using a ULVAC PHI 5000 Versa probe III system to assess the chemical composition and oxidation state of the as-synthesized material. The UV-visible absorbance data were collected using a JASCO V-770 UV-visible spectrophotometer. The electrochemical properties of the material were analyzed through techniques such as cyclic voltammetry (CV), Linear sweep voltammetry (LSV), electrochemical impedance spectroscopy (EIS), and chronoamperometry (CA) measurements.

3. Results and discussion

3.1. XRD analysis

Fig. 1 illustrates the X-ray diffraction (XRD) pattern of $\text{Cu}_2\text{S}/\text{MnO}_2$ and $\text{Cu}_3\text{BiS}_3/\text{MnO}_2$ samples, specifically synthesized as CuMn(3:2) and CuMnBi(3:2:2) respectively. Additionally, Fig. S1 exhibits other samples prepared by altering the molar ratios of Cu, Mn, and Bi at 3:2:0, 3:2:0.5,

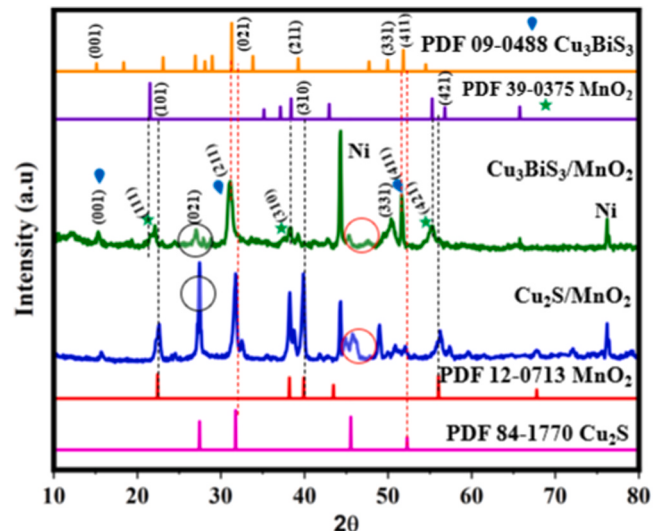


Fig. 1. XRD patterns of $\text{Cu}_2\text{S}/\text{MnO}_2$ and $\text{Cu}_3\text{BiS}_3/\text{MnO}_2$ for the CuMn(3:2) and CuMnBi(3:2:2) samples.

3:2:1, 3:2:2, and 3:2:3. The patterns indicate the simultaneous presence of characteristic diffraction peaks corresponding to the phases of Cu_3BiS_3 fitted to PDF 09-0488 and MnO_2 to PDF 39-0375, without any additional peaks. For the Cu_3BiS_3 phase, the five most intensified diffraction peaks appear around 15.3, 27.1, 30.9, 50.4, and 51.6 degrees, corresponding to the (001), (211), and (411) crystalline planes of the orthorhombic Wittichenite phase, respectively. Regarding MnO_2 , three major diffraction peaks are observed at approximately 22.1, 38.3, and 55.2 degrees, which correspond to the (101), (310), and (421) crystalline planes of the orthorhombic Ramsdellite phase, respectively. Without adding the third metal Bi, the binary CuMn(3:2) catalyst formed two phases of cubic Cu_2S fitted to PDF 84-1770, and uncommon MnO_2 fitted well to PDF 12-0713. In adding the Bi component, the Cu_2S converted to Cu_3BiS_3 and the MnO_2 to the Ramsdellite phase as supported by the peak positions shifted towards lower angles, marked by the dashed lines, and the peak intensity lowered at ~28 and 46 degrees.

MnO_2 is found to exhibit a variety of crystallographic structures, namely $\gamma\text{-MnO}_2$ [44], $\alpha\text{-MnO}_2$ [45], and $\beta\text{-MnO}_2$ [46]. In this work, when subjected to co-precipitation with Cu_3BiS_3 , MnO_2 transforms into the uncommon Ramsdellite phase. This interaction with Cu_3BiS_3 causes MnO_2 a significant departure from its usual face-centered Rocksalt lattice to adopt the orthorhombic arrangement instead. This finding highlights the crucial role of the complicated co-precipitation in shaping the final crystallographic structure of MnO_2 . Fig. S2 provides additional support for the crystal structure formation of Cu_3BiS_3 , as evidenced by the peak formation when the amount of the third metal Bi precursor increased from 0.5 mmol to 3 mmol. This observation further confirms the formation of Cu_3BiS_3 .

3.2. Morphology and surface chemical states of as-prepared electrocatalysts

Fig. 2 presents SEM and TEM images of the synthesized electrochemical catalyst of $\text{CuMnBi}(3:2:2)$. Fig. 2(a) displays the SEM topographic image of the Cu_3BiS_3 and MnO_2 phases, which are randomly distributed and interconnected. EDX composition analysis at the point analysis mode confirms that the smaller rod-like structures are composed of Cu_3BiS_3 , while the rectangular-like structure consists of MnO_2 . In Fig. 2(b), the TEM image reveals the intimate contact between the MnO_2 rectangular and Cu_3BiS_3 smaller nanorods, indicating the presence of two mixed-phase structures. This observation aligns with the aggregated nanorod structure seen in the SEM image (Fig. 2(a)). The lattice fringes in Fig. 2(c) exhibit a d-spacing of 0.31 nm corresponding to the (131) lattice plane of Cu_3BiS_3 . In comparison, Fig. 2(d) shows a d-spacing of 0.20 nm related to the (101) lattice plane of MnO_2 . The HR-TEM images of Cu_3BiS_3 and MnO_2 further confirm the close contact at the heterojunction. In addition, the HR-TEM data aligns with the XRD data, solidifying the identification of a heterojunction composite electrocatalyst. The selected area and the electron beam diffraction are shown in Fig. 2(e) and (f), respectively. The weak diffraction indicates that the catalysts were not in good crystallinity. Moreover, Fig. S3 show the interfacial structure of $\text{Cu}_3\text{BiS}_3/\text{MnO}_2$. The observed lattice spacing of $d = 0.31$ nm corresponds to the (211) Miller indices of Cu_3BiS_3 , while the $d = 0.23$ nm spacing aligns with the (101) Miller indices of MnO_2 . The zone between Cu_3BiS_3 and MnO_2 does not show the sharp grain

boundary but shows the lattice fringes for an ordered structure across the zone. The ordered structure at the $\text{Cu}_3\text{BiS}_3/\text{MnO}_2$ interface provides supporting information for the over-saturation precipitation of MnO_2 from Cu_3BiS_3 due to the mismatch of Mn in the Cu-Bi-S system. As the formation of Cu_3BiS_3 has consumed most of the sulfur precursor, the precipitated Mn is oxidized in the water-based solution to form epitaxial MnO_2 . Fig. S4 provides (a) TEM and (b) SEM energy-dispersive spectroscopy (EDS) analyses, verifying the presence of each element. Notably, no nitrogen elements were detected, indicating the absence of nitrate or nitrite on catalysts. The elemental mapping images of the as-synthesized electrocatalyst from TEM-EDS (Fig. 2(g)–(k)) demonstrate uniform dispersion of Bi, Mn, Cu, S, and O elements within the sample.

X-ray photoelectron spectroscopy (XPS) technique was used to analyze the formation of $\text{Cu}_3\text{BiS}_3/\text{MnO}_2$ and determine the chemical states of each element. The wide-scan XPS spectra in Fig. S5 show the presence of C, Cu, Bi, S, Mn, and O in $\text{Cu}_3\text{BiS}_3/\text{MnO}_2$. The C 1 s peak at 476.2 eV is attributed to the adventitious carbon species in the XPS instrument. The high-resolution XPS spectrum of Bi 4 f in $\text{Cu}_3\text{BiS}_3/\text{MnO}_2$ (Fig. 3(a)) displayed two strong peaks at 157.8 and 159.2 eV, corresponding to $\text{Bi} 4 f_{7/2}$ for Bi^{3+} and Bi^{5+} , respectively. Similarly, the two strong peaks at 163 and 164.3 eV corresponded to $\text{Bi} 4 f_{5/2}$ for Bi^{3+} and Bi^{5+} , respectively. The molar contents of Bi^{3+} and Bi^{5+} were determined to be 62.9 % and 37.1 %, respectively. The S 2p XPS pattern exhibited two peaks at 161.7 eV and 160.6 eV, corresponding to $\text{S} 2p_{1/2}$ and $\text{S} 2p_{3/2}$, respectively, supporting the presence of sulfide in $\text{Cu}_3\text{BiS}_3/\text{MnO}_2$ and its linkage with bismuth. In the Cu^{1+} 2p region (Fig. 3(b)), the peaks corresponding to $\text{Cu} 2p_{1/2}$ and $\text{Cu} 2p_{3/2}$ were observed at 952 eV and 932.5 eV, respectively. The Mn 2p peaks in Fig. 3(c) show their binding energy centers at 639, 643, and 645.8 eV for Mn^{2+} , Mn^{3+} , and Mn^{4+} , respectively. The molar contents of Mn^{2+} , Mn^{3+} , and Mn^{4+} in MnO_2 were determined to be 31.2 %, 42.9 %, and 25.9 %, respectively. The high-resolution spectrum of O 1 s (Fig. 3(d)) revealed three components with binding energy centered at 532.3 eV (surface hydroxide, OH), 531 eV (oxygen vacancy, O_v), and 529.8 eV (lattice oxygen, O_L) with the molar contents of O_L, O_v, and O_{OH} determined to be 42.2 %, 34 %, and 23.8 %, respectively. The XPS data summary is listed in Table S2.

To explore the stoichiometry of the Cu_3BiS_3 and MnO_2 , the crystals in Fig. 2(a) were examined. The SEM-EDS data are shown in Fig. S6, and the calculation and explanations are shown in Table S3. The fact is that

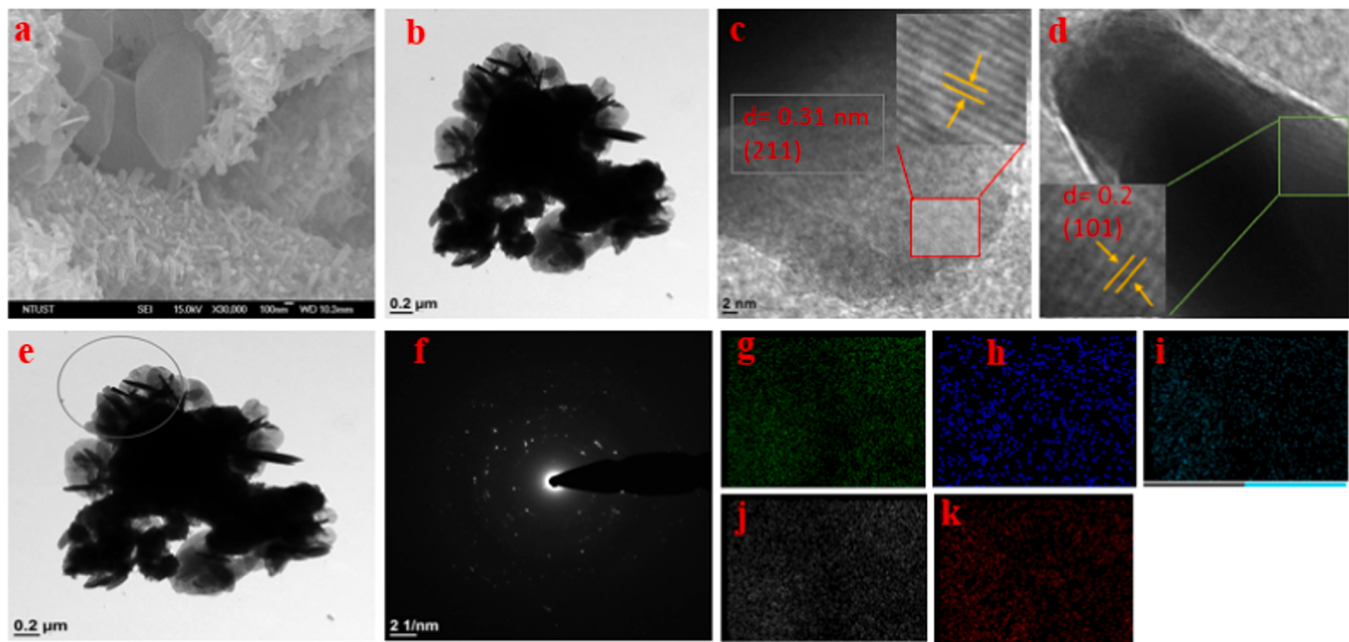


Fig. 2. (a) SEM and (b) TEM images of $\text{Cu}_3\text{BiS}_3/\text{MnO}_2$ from the $\text{CuMnBi}(3:2:2)$ sample. HR-TEM images of (c) Cu_3BiS_3 and (d) MnO_2 . (e and f) The location for diffraction and the diffraction pattern of $\text{CuMnBi}(3:2:2)$. EDS elemental mapping images of (g) Bi, (h) Mn, (i) Cu, (j) S, and (k) O.

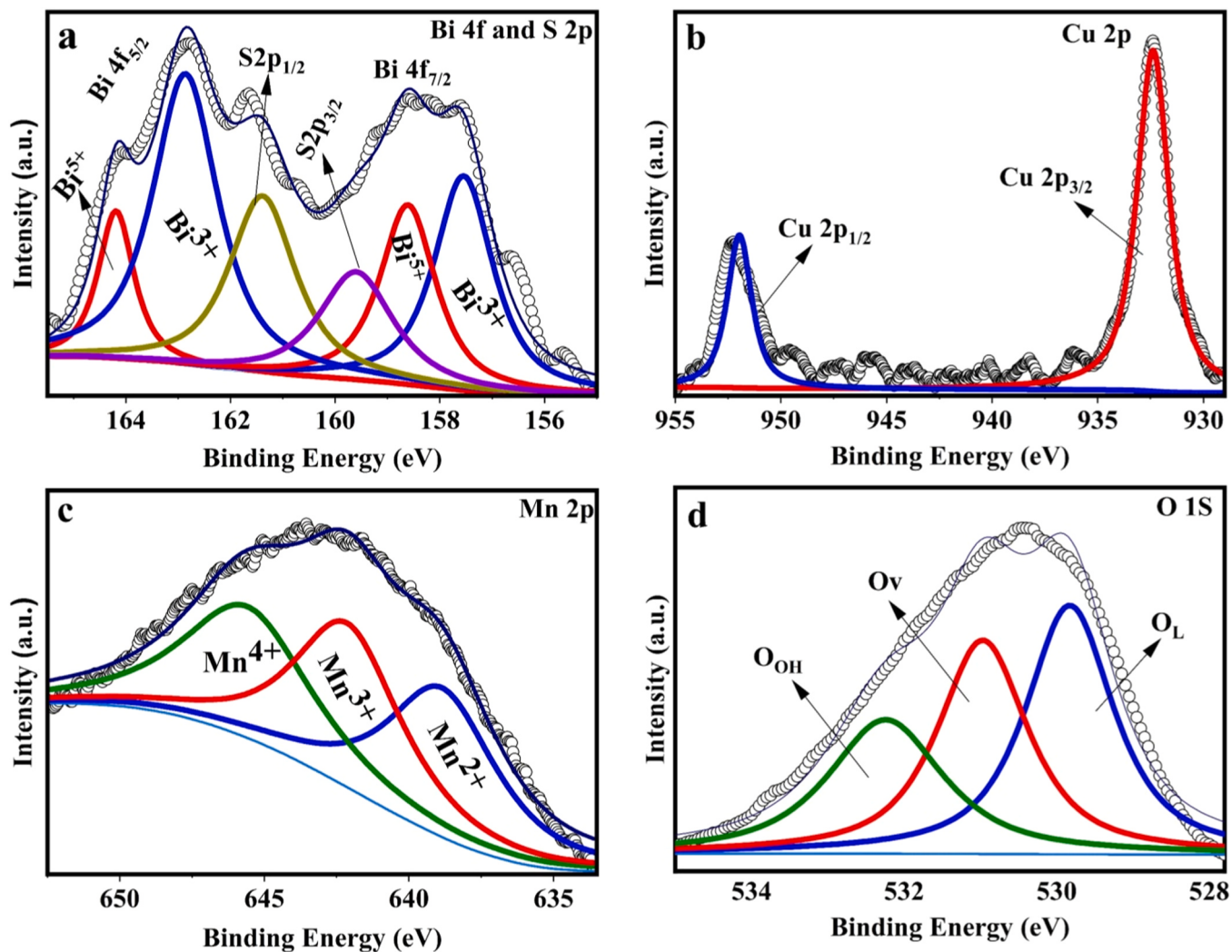


Fig. 3. XPS spectra of (a) Bi 4 f and S 2p, (b) Cu 2p, (c) Mn 2p, and (d) O 1s for the CuMnBi(3:2:2) sample.

the MnO₂ phase contains a small amount of sulfur (Fig. S6) and has little Bi and Cu contents. The Ramsdellite MnO₂ phase can be considered sulfur-doped MnO_{2-y} with 26.3 % oxygen vacancies (V_O). The formed defective (Mn²⁺_{0.312}Mn³⁺_{0.429}Mn⁴⁺_{0.259})O_{2-y} is attributed to the incomplete oxidation of Mn with lots of Mn²⁺ and Mn³⁺, as Mn⁴⁺ is expected for MnO₂. With the sulfur incorporation and the multivalent Mn in MnO₂, a rare Ramsdellite MnO₂ phase forms in this work. For the rod crystals, the components have 19.66 % Cu and 9.17 % Bi, where it has 62.9 % Bi³⁺ and 37.1 % Bi⁵⁺. The Cu₃BiS₃ phase can be viewed as oxygen-doped Cu_{19.66}¹⁺(Bi_{0.629}³⁺Bi_{0.371}⁵⁺)_{9.17}O_{26.987}, 9.17 O-Cu_{2.14}¹⁺(Bi_{0.629}³⁺Bi_{0.371}⁵⁺)S_{2.943} or 9.17 O-Cu_{3-x}BiS₃. There are 58 mol.% MnO_{2-y} and 42 mol.% Cu_{3-x}BiS₃. Therefore, our composite catalyst system of Cu_{3-x}BiS₃/MnO_{2-y} catalyst is highly defective. Those different point defects on lattices are expected to substantially distort the crystals, create effective charges, generate the charge-charge and charge-dipole interactions, enhance the catalyst activity by increasing the entropy-related free energy, etc. To support the highly defective structures with lattice distortion, the high-resolution XPS spectra of Cu₃BiS₃/MnO₂ are compared with the individuals of Cu₃BiS₃ and MnO₂, as shown in Fig. S7. The Cu and O peaks have apparent shifts after adding the Mn precursor into the reaction system, indicating the changes in the surrounding bonding. The important message is the huge shift of the O peaks, which can support the phenomenon of the over-saturation precipitation to built a large stress without stress relaxation by the loose grain boundary.

3.3. Electrochemical performance of ammonia synthesis from nitrogen gas

3.3.1. Optimization of potential and electrolyte

This study investigated the electrochemical performance of Cu₃BiS₃/MnO₂ catalysts of a ternary metal Cu-Bi-Mn compound system synthesized at 160 °C with different metal-precursor ratios for eNRR operated at ambient temperature and pressure conditions. Before the eNRR test, control experiments in different gases have to be performed, as shown in Fig. S8. The ammonia production was measured using two methods: the Nessler's reagent method and the indophenol blue method, as shown in Fig. S9. A steady increase in ammonia concentration over time, indicating continuous reduction with the continuous input of N₂ gas. The absence of fluctuations in ammonia production suggests that the catalyst remained uncontaminated by nitrate sources. After confirming with the Ar-environment baseline test, we have to point out the importance of measuring ammonia yields at different time intervals instead of using the one-time measurement over the whole period. The data trend in the yield vs. time plot can be used to judge the reaction path and electrocatalyst degradation.

Fig. 4(a) shows the results of the eNRR electrocatalysis at different potentials. The average NH₃ yield rates of CuMnBi(3:2:2) are 1372, 3014, 3378, 3604, 3415, and 3053 µg h⁻¹cm⁻² yield rates at -0.25, -0.55, -0.65, -0.75, -0.85, and -0.95 V, respectively, while their respective Faradaic efficiency values are 10.2, 17.4, 22.3, 31.4, 26.7, and 18.3 %. It was found that the CuMnBi(3:2:2) catalyst achieved the

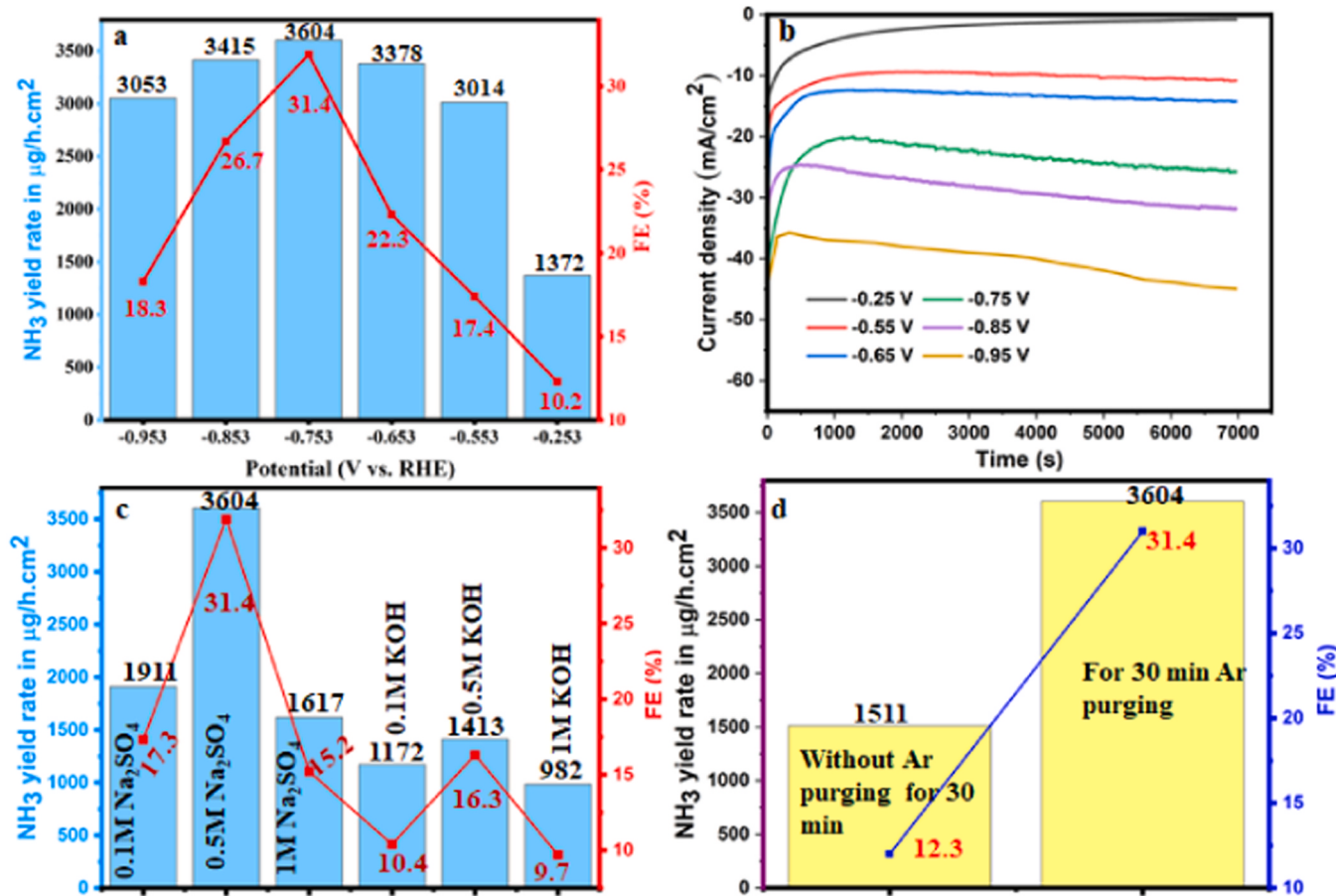


Fig. 4. (a) NH₃ yield with %FE at different potentials. (b) Chronoamperometric data at different test conditions. (c) The electrolyte effect and (d) the environmental effect on the NH₃ performance of CuMnBi(3:2:2).

highest NH₃ yield rate of 3604 μg h⁻¹cm⁻² at -0.75 V vs. RHE and a high FE of 31.4 %. As CuMnBi(3:2:2) has a catalyst loading of 2.51 mg on a Ni foam of 1×1 cm², its average NH₃ yield rate in terms of catalyst weight is 1436 μg h⁻¹mg⁻¹ (Fig. S7). The performance degraded at the condition above -0.75 V. The intense competition from HER primarily causes the lower FE at -0.95 V vs. RHE. Fig. 4(b) displays the variations in chronoamperometry measurements with varying potential. The chronoamperometry curves, conducted under an N₂ atmosphere, exhibited a slight initial decay in current density, particularly at more negative potentials. This decay is attributed to the reduction of the catalyst surface during the electro-reduction process [39]. The chronoamperometric data showed more negative current densities as the applied reduction potential increased from 0.25 V to 0.95 V vs. RHE. To evaluate the electrolyte effect on the colorimetry using the Nessler's reagent, the Na₂SO₄ and KOH electrolytes of 200 ppm used in this work were added individually to a NH₄Cl solution with stirring for 2 h, the same as the electrocatalysis duration, before adding the Nessler's reagent. Fig. S10 clearly shows that different electrolytes in the NH₄Cl solution did not differ in the determination of the ammonia concentration from the pure NH₄Cl standard solution. Then, the NH₃ yields were evaluated at different electrolyte conditions. The highest NH₃ yield rate of 3604 μg h⁻¹cm⁻² was achieved in a 0.5 M Na₂SO₄ electrolyte solution at -0.75 V vs. RHE, which were 1.89- and 2.23-fold higher than the tests in 0.1 M (1911 μg h⁻¹cm⁻²) and 1 M Na₂SO₄ (1617 μg h⁻¹cm⁻²). The NH₃ yields for tests in a KOH solution of 0.1, 0.5, and 1 M are 1172, 1413, and 982 μg h⁻¹cm⁻², respectively, while their FEs are 10.4, 16.3, and 9.7 %. So, 0.5 M Na₂SO₄ solution is the preferred electrolyte. The ENRR rate was much lower for the environmental effect, as shown in Fig. 4(d), where the system did not undergo an Ar-purging procedure for

30 min. A competitive reaction with dissolved oxygen is the inhibitory reason. To present the yield data in terms of the catalyst weight, a plot with the different units is shown in Fig. S11.

3.3.2. Performance of eNRR and electrochemical parameter tests

The performance of the eNRR was evaluated under ambient conditions using a two-compartment cell [42]. The cell consisted of a cathode and an anode compartment separated by a Nafion membrane (NB-211) with a 0.5 M Na₂SO₄ electrolyte solution. The cathode cell was purged with the first Ar for 30 min. Then, N₂ gas flew for two consecutive hours. An additional trap containing a 0.5 M Na₂SO₄ batch solution was used to capture any NH₃ present in the electrolyte. The eNRR measurements were carried out starting from using binary CuMn(3:2) and CuMn(2:3) samples as well as on the best-performed binary system with adding the third metal Bi content to form the ternary metal sulfide/oxide systems, which include CuMnBi(3:2:0.5), CuMnBi(3:2:1), CuMnBi(3:2:2), and CuMnBi(3:2:3) samples. The working electrodes were *in situ* grown on Ni-foam, and the potentials were measured for the reversible hydrogen electrode (RHE) scale. Notably, no N₂H₄ was detected after 2 h of electrolysis for all samples, indicating the excellent selectivity of the electrocatalysis toward the complete conversion of N₂ into NH₃. Time-dependent current density curves were recorded for 120 min. The NH₃ yields of the catalysts for 2 h are 892, 1202, 3669, 5188, 6296, 7208, and 5764 μg cm⁻² for CuMn(2:3), CuMn(3:1), CuMn(3:2), CuMnBi(3:2:0.5), CuMnBi(3:2:1), CuMnBi(3:2:2), and CuMnBi(3:2:3), respectively, while their respective Faradaic efficiency values are 4.3, 4.7, 10.3, 14.1, 23.4, 31.4, and 16.7 % (Fig. 5(a) and (b)). Their average yield rates are 446, 601, 1834, 2594, 3148, 3604, and 2882 μg h⁻¹cm⁻². The variation of yield rate with composition covers a wide span from the

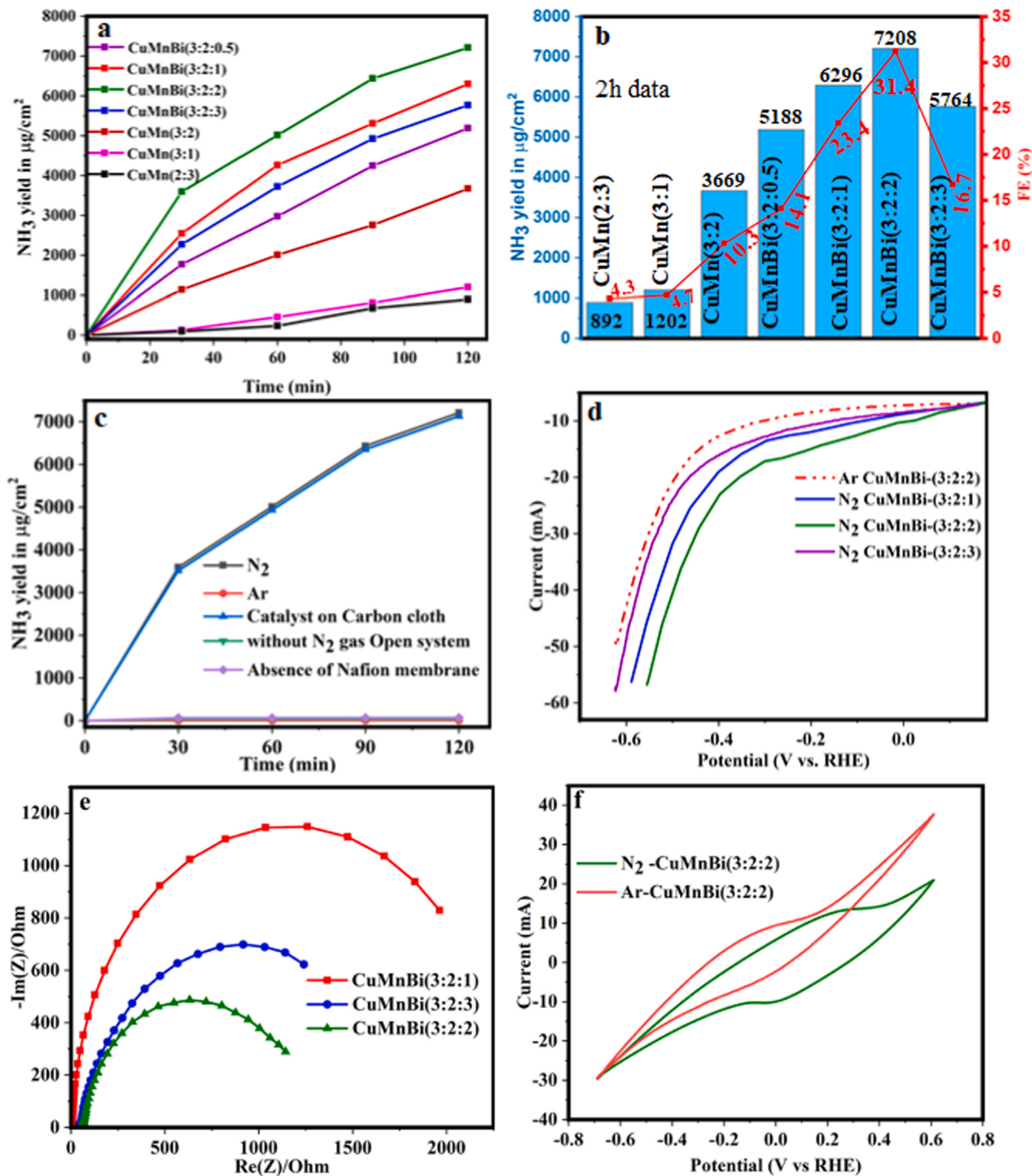


Fig. 5. (a) NH₃ generation at a potential of 0.75 V vs RHE for 2 h. (b) NH₃ generation with %FE at a potential of 0.75 V vs. RHE for 2 h. (c) The control experiments conducted under various conditions. (d) LSV, (e) EIS, and (f) CV tests of the best-performed CuMnBi(3:2:2) catalyst.

low rate of $446 \mu\text{g h}^{-1}\text{cm}^{-2}$ to the high rate of $3604 \mu\text{g h}^{-1}\text{cm}^{-2}$, indicating that eNRR is heavily dependent upon the catalyst composition with the ternary metal compound superior over the binary metal compound. The NH₃ yield rate of CuMnBi(3:2:2) was 8.1 times higher than the low NH₃ yield of CuMn(2:3). To confirm the NH₃ generation, the best-performed CuMnBi(3:2:2) sample was evaluated with the IPB and the Nessler's reagents, as shown in Fig. S12. The NH₃ yields measured by

both of the test methods for the CuMnBi(3:2:2) sample are consistent. Overall, the promising performance of CuMnBi(3:2:2) as an electrocatalyst for eNRR highlights its potential for efficient NH₃ synthesis under ambient conditions.

Our EPR spectroscopy investigation, detailed in Fig. S13, focuses on identifying oxygen vacancies (OVs) in the catalyst, considering their potential influence on the electronic structure of the CuBiMn system

across various ratios. Particularly, a strong EPR signal at $g = 2.000$ in CuMnBi(3:2:2) signifies effective OV-induced generation of unpaired electrons. Comparing EPR signal intensities across samples reveals a trend: CuMnBi(3:2) < CuMnBi(3:2:1) < CuMnBi(3:2:3) < CuMnBi(3:2:2), which is consistent with the NH₃ yield rates in Fig. 5(b). The conclusion is that an optimal VO content leads to the highest NH₃ yield rate. This trend underscores OV impact on the CuMnBi system. Hence, the observed EPR signal intensity in CuMnBi(3:2:2) serves as direct evidence for OV existence, reinforcing the proposed mechanism for improved adsorption.

In our study, we compared the catalytic activity of samples with different composition ratios for eNRR by employing various experimental techniques, including LSV, EIS, and CV, in both Ar- and N₂-saturated environments in a 0.5 M Na₂SO₄ solution. To ensure the accuracy of detecting NH₃ products in the eNRR experiments, we conducted control experiments under different conditions (Fig. 5(c)). The first is to experiment with an Ar atmosphere, which resulted in no production of NH₃ after two hours. The second is to use carbon cloth instead of Ni foam to support the Nafion-binder catalyst powder of the same catalyst weight for eNRR. Interestingly, powder-paste data had the exact eNRR yield, justifying that NF, as an electrical support, was not participating in the eNRR, and thin Nafion film did not block or deactivate the active sites. Thirdly, no NH₃ product was detected when the test was conducted in an open system to the air without the N₂ flow. To understand the importance of the Nafion membrane, we conducted a Nafion-free control experiment with no ammonia production (Fig. 5(c)). Based on these results, we conclude that the investigation proceeding in a membrane reactor is essential for eNRR to avoid the oxidation of the

electrolyte and the products to interfere with the measurements.

The catalytic activities of our ternary metal compound catalysts were compared with the LSV tests (Fig. 5(d)). CuMnBi(3:2:2) exhibited a more significant difference in current densities between N₂-saturated and Ar-saturated eNRR tests, as compared with CuMnBi(3:2:1), CuMnBi(3:2:2), and CuMnBi(3:2:3). This indicates that the ternary metal compound system CuMnBi(3:2:2) has the best activity towards eNRR [47]. The onset potential for the HER of CuMn(3:2) was less negative than CuMn(2:3), indicating that Mn has a favorable HER activity while Cu is relatively poor in HER. Upon incorporating the third metal Bi, CuMnBi(3:2:2) reached the best condition to have the higher current density for producing NH₃. The EIS curves (Fig. 5(e)) give information on the charge transfer resistance of the electrode. CuMnBi(3:2:2) in the high-frequency zone had a much smaller semicircle than others for an accelerated electron transfer rate in CuMnBi(3:2:2). The CV test confirms the favorable reaction occurs in the N₂ atmosphere (Fig. 5(f)). Overall, the CuMnBi(3:2:2) electrode exhibits faster reaction kinetics, a larger electrochemical active area, and better conductivity, indicating its superior performance in eNRR [19,39].

3.4. Stability test

For evaluating the stability of the CuMnBi(3:2:2) electrocatalyst, cyclic experiments were conducted, involving five consecutive cycles of electrocatalysis with each lasting 2 h in a 0.5 M Na₂SO₄ solution at a potential of -0.75 V vs. RHE. The three key parameters, namely current density, NH₃ yield rate, and Faradaic efficiencies, remained unchanged,

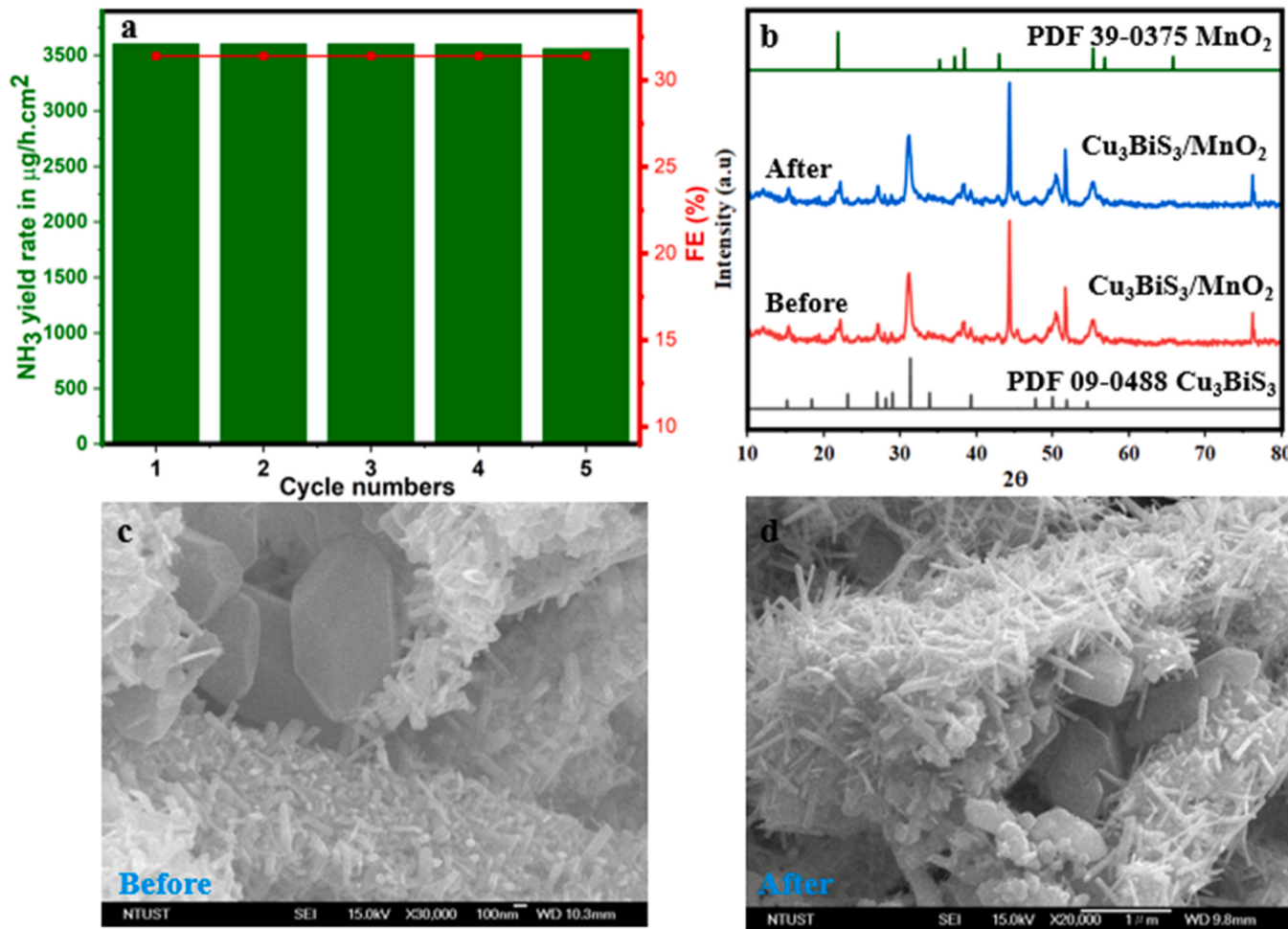


Fig. 6. (a) Five consecutive nitrogen fixation measurements over the CuMnBi(3:2:2) sample. (b) XRD patterns and SEM images (c) before and (d) after the cycled tests for CuMnBi(3:2:2).

highlighting the reliability of CuMnBi(3:2:2) for practical applications (Fig. 6(a)). The cycled catalyst did not change its crystalline structure, as evidenced by the absence of peak shifts or intensity changes for its XRD patterns (Fig. 6(b)). The cycled samples did not change their microstructure, either (Fig. 6(c) and (d)). The CuMnBi(3:2:2) catalyst exhibited efficient and stable electrochemical catalytic performance for eNRR. Moreover, as depicted in Fig. S14 for the chronoamperometric stability experiments, the CuMnBi(3:2:2) catalyst demonstrated effective performance for up to 12 h during continuous reduction processes. Fig. S15 shows XPS data of CuMnBi(3:2:2) before and after a continuous 12 h eNRR stability test. The XPS spectra of CuMnBi(3:2:2) before and after stability tests are similar, suggesting the catalyst's stability over this duration. The overall stability and excellent performance of the CuMnBi(3:2:2) catalyst indicate its potential for sustained and reliable eNRR.

3.5. The proposed eNRR mechanism

Active surface sites on catalysts have been frequently discussed for understanding the enhanced electrochemical catalytic N₂ fixation. Still, the so-called active sites and the involved reaction mechanisms behind this phenomenon require further investigation. Our as-prepared Cu₃BiS₃/MnO₂ from the CuMnBi(3:2:2) electrocatalyst exhibits excellent eNRR properties to excel in most reported data (Table 1) [27,37–40, 42,48–51], including our work on the ternary metal (Fe-Mn-Ga) and quaternary metal (Ni-V-Mn-Nb) compound systems. Without adding the third metal Bi, the CuMn(3:2) catalyst formed the phases of Cu₂S and MnO₂, but its 2 h eNRR yield already reaches 3669 µg/cm² (Fig. 5(b)) and is much higher than other reports (Table 1). With increasing Bi content, the new phase forms and the 2 h yield reaches its highest at 7208 µg/cm². When the Bi addition into the CuMn system is a crucial factor in increasing the eNRR rate to the highest, we should not forget the CuMn(3:2) electrocatalyst is already important. Supported by the EPR data in Fig. S13 with the trend similar to the NH₃ yield rate, the eNRR kinetic mechanism involves the environment created by the precipitated phases. The approach of adsorption energy from the element contribution is not suitable to be applied here. Based upon the overall data, we propose that the MnO₂ phase in the CuMn(3:2) catalyst contributes the first part of the active VO sites to reach a high NH₃ yield rate, followed by the formation of the Cu₃BiS₃ phase with the Bi addition to create the second part of active VO sites and to further increase the yield rate to the highest. The VO-based kinetic mechanism is based upon the two highly defective phases of Cu₃BiS₃ and MnO₂, as explained below.

Comprehensive phase and composition analyses of CuMnBi(3:2:2) were conducted to gain deeper insights. In this case, our Cu₃BiS₃/MnO₂ sample involves two defects-complicated compounds with severe non-stoichiometry: the Cu-deficient Cu_{3-x}BiS₃ with Bi at the Bi³⁺ and Bi⁵⁺ valence states and the oxygen-deficient MnO_{2-y} with Mn at the Mn²⁺,

Mn³⁺, and Mn⁴⁺ valence states. It is rare to have Bi consisting of two valence states. With Cu in deficiency as the driving force, the Bi³⁺ must be converted into Bi⁵⁺ to compensate for the positive charge loss and keep the total amount neutral. Here, we emphasize that Cu_{3-x}BiS₃ is an ionic compound with strong Coulombic interaction to form a crystal. Although the Cu_{3-x}BiS₃ compound is expressed, its point defects are very complex, including the negatively charged Cu vacancy (V_{Cu}¹⁻) defect and the positively charged Bi⁵⁺-on-Bi³⁺ defect (Bi_{Bi}²⁺) at the atomic level coexist. The formation of two Cu vacancies accompanies the generation of one Bi⁵⁺ defect. The negatively charged V_{Cu}¹⁻ defects and the positively charged Bi_{Bi}²⁺ defects are uniformly distributed and form many localized electrical nano dipoles on an atomic scale in Cu_{3-x}BiS₃. It is also rare to have Mn consisting of the three valence states. MnO_{2-y} has the positively charged oxygen vacancy (V_O²⁺) defects, and the negatively charged Mn²⁺-on-Mn⁴⁺ (Mn_{Mn}²⁻) and Mn³⁺-on-Mn⁴⁺ defects (Mn_{Mn}¹⁻). To balance the drop in the total positive valence charge due to the formation of Mn²⁺ and Mn³⁺, the accompanying defect of oxygen vacancy forms. There are also many electrical nano dipoles in MnO_{2-y}. Although the 58 mol.% MnO_{2-y} showed a large crystal size of 2–3 µm and had a smooth surface, it should have excellent eNRR activity for obtaining the best CuMnBi(3:2:2) electrocatalyst. The reason for MnO_{2-y} with perfect catalyst activity can be attributed to the atomic point defects and nano dipoles.

The significant jump in the ammonia yield involves the enhanced N≡N adsorption on the inorganic catalyst. Traditional surface adsorption involves the dissociative and associative pathways, but adsorption involving the p-d orbital interaction is very localized without considering the total crystal complexity, surroundings, and defect atmosphere. For example, Cu_{3-x}BiS₃ has Cu vacancy and Bi⁵⁺ point defects, and MnO_{2-y} has Mn²⁺, Mn³⁺, Mn⁴⁺, and oxygen vacancy. Those atoms at different states have different behaviors, which have yet to be considered as factors for the material computation in such complicated compounds. Our eNRR kinetic reaction intends to be presented differently from the available reports. As N₂ is inert, has a triple bond, has no dipole, and has no solubility in an aqueous solution, the most critical step for a successful eNRR process is the intense trapping or chemical adsorption of the easily escaped N₂ gas by the catalyst, which determines the dwelling duration of the N₂ adsorbates. To have the kinetic mechanism fitted to our experimental data with excellent performance after converting from a binary to a ternary metal compound system, the created complex defects in our Cu_{3-x}BiS₃/MnO_{2-y} composite catalyst play crucial roles from our viewpoint. We propose here that the positively charged ends of Bi_{Bi}²⁺ at a Bi_{Bi}²⁺–V_{Cu}¹⁻ nano dipole and V_O²⁺ at a V_O²⁺–Mn_{Mn}²⁻ nano dipole in Cu_{3-x}BiS₃ and MnO_{2-y} respectively, to initiate the interaction between N₂ and catalyst, to attract the lone-paired electrons from N₂, to trap and distort the electron cloud of N₂, and to

Table 1
Recent studies on electrocatalysis for efficient N₂ fixation by heterostructure-based nanocomposites.

No.	Catalyst	Synthesis method	Potential vs. RHE (V)	Electrolyte	Yield rate in µg/h.cm ²	%FE	Ref.
1	Cu ₃ BiS ₃ /MnO ₂	Hydrothermal	−0.75	Na ₂ SO ₄	3604	31.4	This work [27]
2	Pt/TiO _x	Laser+ Hydrothermal	−0.2	NaOH	91.0	1.57	[27]
3	BiVO ₄ /TiO ₂	Hydrothermal	−0.8	Na ₂ SO ₄	8.54	7.70	[37]
4	1 T-MoS ₂ /MoO ₃	Hydrothermal	−0.2	H ₂ SO ₄	41.47	18.9	[38]
5	Cu _{2-x} S/MoS ₂	Room temp.	−0.5	Na ₂ SO ₄	1.77	6.06	[39]
6	FeS ₂ /MoS ₂	Hydrothermal	−0.3	Na ₂ SO ₄	4.40	4.63	[40]
7	(Fe,Mn,Ga) ₃ O _{4-x} /(Mn,Fe) ₂ O _{3-y}	Hydrothermal	−0.6	Na ₂ SO ₄	2036	5.77	[42]
8	TiO ₂ /Ag/Cu ₇ S ₄ @Se-CC	Hydrothermal	−0.3	KOH	39.16	51.05	[48]
9	1 T MoS ₂ /g-C ₃ N ₄	Thermal+ Hydrothermal	−0.5	Na ₂ SO ₄	60.3	21.01	[49]
10	V ₂ O ₅ /VN	Hydrothermal+Thermal	−0.4	H ₂ SO ₄	23.9	34.9	[50]
11	Mn _{Ni0.5V1.5O4} / (Ni,V,Mn) ₃ O ₄	Hydrothermal	−0.5	Na ₂ SO ₄	3190	22.7	[51]

polarize the N₂ molecule for an easy hydrogenation reaction from the aid of the protons transporting from the anode through the water oxidation. The proposed kinetic micromechanism to describe the interaction between N≡N and nano dipoles is schematically presented in Fig. 7. This surface defect atmosphere concept is similar to the dislocation to interact with solutes for forming a dislocation atmosphere. Once the N₂ molecule starts its polarization after interacting with the defect- or nano dipole-filled atmosphere, the N₂ dipole-catalyst dipole interaction becomes more robust, with the negatively charged ends of the nano dipoles interacting with the positive end of N₂, and the N₂ triple bond becomes weakened. The stabilization with the formation of the N-H bond via the proton-adding reduction reaction further accelerates the N₂-involved inert reaction. The kinetic reactions can be simplified as listed below.

Step 1. N₂ adsorption and polarization at cathode::N≡N: + Bi_{Bi}²⁺/V_O²⁺



Step 2. Water oxidation at anode: H₂O → H⁺ + $\frac{1}{2}$ O₂ + e⁻

Step 3. Hydrogenation reaction of weakened N₂: $\oplus\text{N}\equiv\text{N}\text{-Bi}_{\text{Bi}}^{2+}/\text{V}_{\text{O}}^{2+}$ + 6 H⁺ + 6 e⁻ → 2 NH₃

Step 4. Hydrolysis of NH₃: NH₃ + H₂O → NH_{3(aq)}⁺ + OH⁻

Creating highly defective compounds with multiple charged valences by the complicated reactions among the ternary metal precursors at a mild condition is the origin of eNRR performing excellent with an average yield rate of 3604 µg h⁻¹cm⁻² or 1436 µg h⁻¹mg⁻¹ and Faradaic efficiency of 31.4 %. In addition to the enhanced N₂ trapping capability, the Cu_{3-x}BiS₃/MnO_{2-y} catalyst has lowered its charge transfer resistance by adding the third metal of Bi. The enriched defects lead to the improved electrical conductivity. A charge transfer polaron mechanism is applied on the Cu_{3-x}BiS₃/MnO_{2-y} catalyst. Each point defect of V_{Cu}¹⁻, Bi_{Bi}²⁺, Mn_{Mn}²⁻, Mn_{Mn}¹⁻, or V_O²⁺ has its polaron size, depending upon the electron trapping state on defects. By adjusting the third metal Bi

content to optimize the defect concentration (Fig. 5(e)) and the polaron concentration, the easy charge transport with low electrical resistance becomes available through the charge hopping between polarons with the aid of the applied voltage to initiate the interaction. Overall, this comprehensive eNRR process involves nitrogen fixation and activation, protonation, nitrogen reduction, and ammonia desorption, enabling the conversion of nitrogen gas into ammonia on the defects-rich surface of Cu₃BiS₃/MnO₂ catalysts.

4. Conclusions

A novel ternary metal Cu-Mn-Bi electrocatalyst system of Cu₃BiS₃/MnO₂ sulfide/oxide with multiple cation and anion point defects was successfully synthesized using a simple one-step hydrothermal process to be deposited on Ni foam support for the electrocatalytic nitrogen reduction reaction (eNRR). With inserting the third metal element Bi into CuMn(3:2), the performance of the CuMnBi(3:2:2) catalyst was significantly improved compared to its binary counterpart. The electrocatalytic generation of NH₃ followed the order: CuMnBi(3:2:2) > CuMnBi(3:2:1) > CuMnBi(3:2:3) > CuMnBi(3:2:0.5) > CuMn(3:2) with the highest rate of 3604 µg h⁻¹cm⁻² or 1436 µg h⁻¹mg⁻¹ and the high Faradaic efficiency of 31.4 %. CuMnBi(3:2:2) catalyst demonstrated exceptional stability, retaining 100 % of its original activity after 10 h of operation. By harnessing point defects of V_{Cu}¹⁻, Bi_{Bi}²⁺, Mn_{Mn}²⁻, Mn_{Mn}¹⁻, and V_O²⁺ in CuMnBi(3:2:2), novel metal- and nonmetal-defective Cu_{3-x}BiS₃ and MnO_{2-y} were created and accompanied by nano dipoles, highlighting the significance of solid solution engineering in ionic solids for developing unconventional catalysts. The defects-formed nano dipole atmosphere provides strong trapping sites for the easily escaped N₂ to overcome the bottleneck reaction of firm adsorption in eNRR. This study provides valuable insights into designing and preparing highly efficient catalysts for eNRR through the complex reactions of multiple metal precursors at mild conditions.

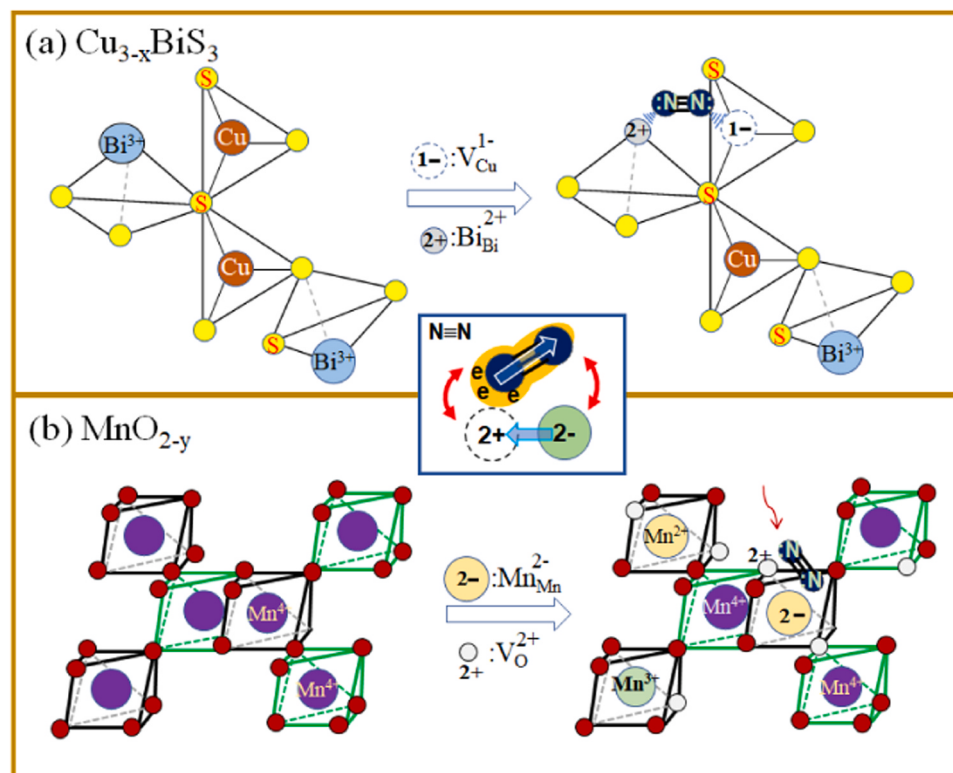


Fig. 7. The N₂-nano dipole interaction micromechanism to weaken the inert N₂ triple bond for forming ammonia.

CRediT authorship contribution statement

Tadele Negash Gameda: Methodology, Investigation, Conceptualization. **Quoc-Nam Ha:** Methodology, Investigation, Formal analysis. **Noto Susanto Gultom:** Methodology, Formal analysis. **Merga Hailemariam Urgesa:** Writing – original draft, Methodology, Investigation, Formal analysis, Data curation, Conceptualization. **Dong-Hau Kuo:** Writing – review & editing, Writing – original draft, Supervision, Resources, Project administration, Investigation, Funding acquisition, Conceptualization.

Declaration of Competing Interest

The authors declare that they have no known competing financial interests or personal relationships that could have appeared to influence the work reported in this paper.

Data Availability

The data that has been used is confidential.

Acknowledgments

This work was supported by the National Science and Technology Council (NCST), Taiwan, under grant numbers MOST-110-2221-E-011-038-MY3 and MOST 110-2221-E-011-100-MY3.

Appendix A. Supporting information

Supplementary data associated with this article can be found in the online version at doi:10.1016/j.apcatb.2024.124194.

References

- [1] M.H. Urgesa, G.S. Wolde, D.-H. Kuo, Plasmonic silver nanoparticle-deposited n-Bi₂S₃/p-MnOS diode-type catalyst for enhanced photocatalytic nitrogen fixation: introducing the defective p-MnOS, Chem. Eng. J. 464 (2023) 142717.
- [2] M.H. Urgesa, G.S. Wolde, D.-H. Kuo, One-step hydrothermal synthesis of novel flower-like Bi₂Mn₄O₁₀ anchored on BiOI_{1-x}Br_x nanosheets for efficient photocatalytic nitrogen fixation, J. Alloys Compd. 947 (2023) 169589.
- [3] O. Herbinet, P. Bartocci, A.G. Dana, On the use of ammonia as a fuel—a perspective, Fuel Commun. 11 (2022) 100064.
- [4] C. Kurien, M. Mittal, Review on the production and utilization of green ammonia as an alternate fuel in dual-fuel compression ignition engines, Energy Convers. Manag. 251 (2022) 114990.
- [5] C. Sun, X. Fan, Y. Li, H. Han, J. Zhu, L. Liu, X. Geng, Research on the offshore adaptability of new offshore ammonia-hydrogen coupling storage and transportation technology, Renew. Energy 201 (2022) 700–711.
- [6] L. Ouyang, J. Jiang, K. Chen, M. Zhu, Z. Liu, Hydrogen production via hydrolysis and alcoholysis of light metal-based materials: a review, Nano-Micro Lett. 13 (2021) 134.
- [7] S. Wu, N. Salmon, M.M.-J. Li, R. Bañares-Alcántara, S.C.E. Tsang, Energy decarbonization via green H₂ or NH₃? ACS Energy Lett. 7 (2022) 1021–1033.
- [8] C. Feng, J. Liu, Q. Li, L. Ji, P. Wu, X. Yuan, H. Hu, H.Y. Jiang, G. Xue, Fabricating Ag/PW₁₂/Zr-mTiO₂ composite via doping and interface engineering: an efficient catalyst with bifunctionality in photo-and electro-driven nitrogen reduction reactions, Adv. Sustain. Syst. 6 (2022) 2100307.
- [9] Z. Han, P. Wu, M. He, X. Zhuang, H. Lin, S. Han, Ammonia synthesis by electrochemical nitrogen reduction reaction—a novel energy storage way, J. Energy Storage 55 (2022) 105684.
- [10] F. Tavella, D. Giudi, C. Ampelli, Nitrogen reduction reaction to ammonia at ambient conditions: a short review analysis of the critical factors limiting electrocatalytic performance, Curr. Opin. Green Sustain. Chem. 35 (2022) 100604.
- [11] S. Chen, Z. Zhou, B. Bai, Z. Dai, J. Shi, In-situ-generated MoO₂ on MoS₂/ZnO heterostructures with enriched S, O-vacancies for enhanced electrocatalytic reduction of N₂ to NH₃, ChemElectroChem 9 (2022) e02200625.
- [12] K. Chu, Q.-Q. Li, Y.-P. Liu, J. Wang, Y.-H. Cheng, Filling the nitrogen vacancies with sulphur dopants in graphitic C₃N₄ for efficient and robust electrocatalytic nitrogen reduction, Appl. Catal. B: Environ. 267 (2020) 118693.
- [13] C. He, Z.-Y. Wu, L. Zhao, M. Ming, Y. Zhang, Y. Yi, J.-S. Hu, Identification of FeN₄ as an efficient active site for electrochemical N₂ reduction, ACS Catal. 9 (2019) 7311–7317.
- [14] U.K. Ghorai, S. Paul, B. Ghorai, A. Adalder, S. Kapse, R. Thapa, A. Nagendra, A. Gain, Scalable production of cobalt phthalocyanine nanotubes: efficient and robust hollow electrocatalyst for ammonia synthesis at room temperature, ACS Nano 15 (2021) 5230–5239.
- [15] L. Shi, Y. Yin, S. Wang, X. Xu, H. Wu, J. Zhang, S. Wang, H. Sun, Rigorous and reliable operations for electrocatalytic nitrogen reduction, Appl. Catal. B: Environ. 278 (2020) 119325.
- [16] S. Murmu, S. Paul, S. Kapse, R. Thapa, S. Chattopadhyay, N. Abharana, S.N. Jha, D. Bhattacharyya, U.K. Ghorai, Unveiling the genesis of the high catalytic activity in nickel phthalocyanine for electrochemical ammonia synthesis, J. Mater. Chem. A 9 (2021) 14477–14484.
- [17] H. Zhao, Z.-Y. Yuan, Surface/interface engineering of high-efficiency noble metal-free electrocatalysts for energy-related electrochemical reactions, J. Energy Chem. 54 (2021) 89–104.
- [18] N. Wang, P. Ou, R.K. Miao, Y. Chang, Z. Wang, S.-F. Hung, J. Abed, A. Ozden, H.-Y. Chen, H.-L. Wu, Doping shortens the metal/metal distance and promotes OH coverage in non-noble acidic oxygen evolution reaction catalysts, J. Am. Chem. Soc. 145 (2023) 7829–7836.
- [19] B. Chang, H. Yuan, L. Li, J. Yu, X. Liu, W. Yu, B. Wang, L. Zhao, X. Liu, S. Sun, Enhancing electrochemical nitrogen fixation by mimicking π back-donation on laser-tuned Lewis acid sites in noble-metal-molybdenum carbide, Appl. Catal. B: Environ. 320 (2023) 121777.
- [20] J. Hu, A. Al-Salihy, B. Zhang, S. Li, P. Xu, Mastering the D-band center of iron-series metal-based electrocatalysts for enhanced electrocatalytic water splitting, Int. J. Mol. Sci. 23 (2022) 15405.
- [21] X. Liu, H. Xie, X. Qu, K. Yu, H. Yin, Q. Song, Z. Ning, Electrochemical potential controlling preparation of oxygen vacancies modified SrTiO₃ with Ti³⁺ and Ti²⁺ self-doping in molten salt, J. Solid State Chem. 302 (2021) 122387.
- [22] Y. Xu, X. Liu, N. Cao, X. Xu, L. Bi, Defect engineering for electrocatalytic nitrogen reduction reaction at ambient conditions, Sustain. Mater. Technol. 27 (2021) e00229.
- [23] P.-Y. Liu, K. Shi, W.-Z. Chen, R. Gao, Z.-L. Liu, H. Hao, Y.-Q. Wang, Enhanced electrocatalytic nitrogen reduction reaction performance by interfacial engineering of MOF-based sulfides FeNi₂S₄/NiS hetero-interface, Appl. Catal. B: Environ. 287 (2021) 119956.
- [24] Y. Wan, J. Xu, R. Lv, Heterogeneous electrocatalysts design for nitrogen reduction reaction under ambient conditions, Mater. Today 27 (2019) 69–90.
- [25] D. Yan, H. Li, C. Chen, Y. Zou, S. Wang, Defect engineering strategies for nitrogen reduction reactions under ambient conditions, Small Methods 3 (2019) 1800331.
- [26] R. Hao, W. Sun, Q. Liu, X. Liu, J. Chen, X. Lv, W. Li, Y. Liu, Z. Shen, Efficient electrochemical nitrogen fixation over isolated Pt sites, Small 16 (2020) 2000015.
- [27] J. Lv, Z. Tian, K. Dai, Y. Ye, C. Liang, Interface and defect engineer of titanium dioxide supported palladium or platinum for tuning the activity and selectivity of electrocatalytic nitrogen reduction reaction, J. Colloid Interface Sci. 553 (2019) 126–135.
- [28] Y. Chen, R. Guo, X. Peng, X. Wang, X. Liu, J. Ren, J. He, L. Zhuo, J. Sun, Y. Liu, Highly productive electrosynthesis of ammonia by admolecule-targeting single Ag sites, ACS Nano 14 (2020) 6938–6946.
- [29] W.P. Utomo, M.K.H. Leung, Z. Yin, H. Wu, Y.H. Ng, Advancement of bismuth-based materials for electrocatalytic and photo (electro) catalytic ammonia synthesis, Adv. Funct. Mater. 32 (2022) 2106713.
- [30] Y. Wan, H. Zhou, M. Zheng, Z.H. Huang, F. Kang, J. Li, R. Lv, Oxidation state modulation of bismuth for efficient electrocatalytic nitrogen reduction to ammonia, Adv. Funct. Mater. 31 (2021) 2100300.
- [31] D. Yao, C. Tang, L. Li, B. Xia, A. Vasileff, H. Jin, Y. Zhang, S.Z. Qiao, In situ fragmented bismuth nanoparticles for electrocatalytic nitrogen reduction, Adv. Energy Mater. 10 (2020) 2001289.
- [32] L. Xia, W. Fu, P. Zhuang, Y. Cao, M.O.L. Chee, P. Dong, M. Ye, J. Shen, Engineering abundant edge sites of bismuth nanosheets toward superior ambient electrocatalytic nitrogen reduction via topotactic transformation, ACS Sustain. Chem. Eng. 8 (2020) 2735–2741.
- [33] L. Li, C. Tang, B. Xia, H. Jin, Y. Zheng, S.-Z. Qiao, Two-dimensional mosaic bismuth nanosheets for highly selective ambient electrocatalytic nitrogen reduction, ACS Catal. 9 (2019) 2902–2908.
- [34] S. Santra, V. Streibel, L.I. Wagner, N. Cheng, P. Ding, G. Zhou, E. Sirotti, R. Kisslinger, T. Rieh, S. Zhang, Tuning carbon dioxide reduction reaction selectivity of Bi single-atom electrocatalysts with controlled coordination environments, ChemSusChem (2024) e202301452.
- [35] Z. Fang, P. Wu, Y. Qian, G. Yu, Gel-derived amorphous bismuth–nickel alloy promotes electrocatalytic nitrogen fixation via optimizing nitrogen adsorption and activation, Angew. Chem. 133 (2021) 4321–4327.
- [36] Y. Wang, M.M. Shi, D. Bao, F. Meng, Q. Zhang, Y. Zhou, K. Liu, Y. Zhang, J. Wang, Z. Chen, Generating defect-rich bismuth for enhancing the rate of nitrogen electroreduction to ammonia, Angew. Chem. 131 (2019) 9564–9569.
- [37] Y. Liu, P. Deng, R. Wu, R.A. Geioushy, Y. Li, Y. Liu, F. Zhou, H. Li, C. Sun, BiVO₄/TiO₂ heterojunction with rich oxygen vacancies for enhanced electrocatalytic nitrogen reduction reaction, Front. Phys. 16 (2021) 53503.
- [38] X. Zi, J. Wan, X. Yang, W. Tian, H. Zhang, Y. Wang, Vacancy-rich 1T-MoS₂ monolayer confined to MoO₃ matrix: an interface-engineered hybrid for efficiently electrocatalytic conversion of nitrogen to ammonia, Appl. Catal. B: Environ. 286 (2021) 119870.
- [39] T. Jiang, L. Li, L. Li, Y. Liu, D. Zhang, D. Zhang, H. Li, B. Mao, W. Shi, Ultra-thin shelled Cu_{2-x}S/MoS₂ quantum dots for enhanced electrocatalytic nitrogen reduction, Chem. Eng. J. 426 (2021) 130650.
- [40] B. Wang, C. Yan, G. Xu, X. Shu, J. Lv, J. Cui, D. Yu, Z. Bao, Y. Wu, Electron coupled FeS₂/MoS₂ heterostructure for efficient electrocatalytic ammonia synthesis under ambient conditions, Dalton Trans. 51 (2022) 9720–9727.
- [41] Y. Cui, A. Dong, Y. Qu, J. Zhang, M. Zhao, Z. Wang, Q. Jiang, Theory-guided design of nanoporous CuMn alloy for efficient electrocatalytic nitrogen reduction to ammonia, Chem. Eng. J. 426 (2021) 131843.

- [42] T.N. Gemedo, D.-H. Kuo, G. Sisay Wolde, N.S. Gultom, In situ grown (Fe, Mn, Ga)₃O_{4-x} spinel/(Mn, Fe)₂O_{3-y} bixbyite dual-phase electrocatalyst for preeminent nitrogen reduction to ammonia: a step toward the NH₃ economy, *ACS Appl. Energy Mater.* 6 (2023) 8063–8071.
- [43] D. Gupta, A. Kafle, T.C. Nagaiah, Dinitrogen reduction coupled with methanol oxidation for low overpotential electrochemical NH₃ synthesis over cobalt pyrophosphate as bifunctional catalyst, *Small* (2023) 2208272.
- [44] S. Chou, F. Cheng, J. Chen, Electrodeposition synthesis and electrochemical properties of nanostructured γ-MnO₂ films, *J. Power Sources* 162 (2006) 727–734.
- [45] K. Ahmad, A. Mohammad, S.M. Mobin, Hydrothermally grown α-MnO₂ nanorods as highly efficient low cost counter-electrode material for dye-sensitized solar cells and electrochemical sensing applications, *Electrochim. Acta* 252 (2017) 549–557.
- [46] M. Divagar, R. Sriramprabha, N. Ponpandian, C. Viswanathan, Highly selective and sensitive electrochemical detection of dopamine with hydrothermally prepared β-MnO₂ nanostructures, *Mater. Sci. Semicond. Process.* 83 (2018) 216–223.
- [47] H. Zhang, R. Lv, Defect engineering of two-dimensional materials for efficient electrocatalysis, *J. Mater.* 4 (2018) 95–107.
- [48] L. Zhang, P.-Y. Liu, W.-Z. Chen, Y. Liu, Z. Liu, Y.-Q. Wang, Multicomponent TiO₂/Ag/Cu₇S₄@Se heterostructures constructed by an interface engineering strategy for promoting the electrocatalytic nitrogen reduction reaction performance, *Inorg. Chem.* 61 (2022) 7165–7172.
- [49] R. Liu, T. Guo, H. Fei, Z. Wu, D. Wang, F. Liu, Highly efficient electrocatalytic N₂ reduction to ammonia over metallic 1T phase of MoS₂ enabled by active sites separation mechanism, *Adv. Sci.* 9 (2022) 2103583.
- [50] X. Yang, J. Wan, H. Zhang, Y. Wang, In situ modification of the d-band in the core-shell structure for efficient hydrogen storage via electrocatalytic N₂ fixation, *Chem. Sci.* 13 (2022) 11030–11037.
- [51] T.N. Gemedo, D.-H. Kuo, Q.-N. Ha, One-step synthesized Nb₂O_{5-y}-decorated spinel-type (Ni,V,Mn)₃O_{4-x} nanoflowers for boosting electrocatalytic reduction of nitrogen into ammonia, *Green. Chem.* 25 (2023) 10498–10512.